Pure appl. geophys. 160 (2003) 2419–2446
0033–4553/03/122419–28
DOI 10.1007/s00024-003-2402-4

Pure and Applied Geophysics

Numerical Simulation of the Response of the Ocean Surface Layer to Precipitation

SHAOWU BAO,[1] SETHU RAMAN,[1] and LIAN XIE[1]

Abstract — Numerical experiments were conducted to investigate the ocean's response to the precipitation. A squall line observed in TOGA COARE was simulated. The simulation reproduced some of the observed ocean responses to the precipitation, such as the formation of a fresh water layer, surface cooling and the variation of upper layer turbulent mixing. The precipitation-induced fresh layer can cause the vertical turbulent diffusivities to decrease from the surface to a depth of about 11–13 meters within a few hours. After the rainfall, the turbulence increases near the surface of the ocean due to the combined effect of increased shear and wind forcing, but decreases with depth due to the development of a stable layer. The main reason for the turbulence variation is the decrease in the vertical turbulence flux below the surface fresh layer because of increased static stability. Sensitivity experiments reveal that the sea-surface temperature increases faster after rainfall due to the formation of a shallow fresh water layer near the surface.

Key words: Air-sea interaction, coupled model, ocean mixed layer.

1. Introduction

The region of the tropical western Pacific that has SST higher than 28 °C is called the western Pacific warm pool. Because of the high SST, the western Pacific warm pool supplies the atmosphere a large amount of heat and moisture that results in substantial annual tropical precipitation. Western Pacific warm pool is a product of regional air-sea interaction and it plays an important role in the global seasonal and inter-annual climate variability such as El Niño and Southern Oscillation (ENSO). Easterly trade winds prevail over most of the western equatorial Pacific. However during boreal winters and springs the easterly trade winds are often interrupted by strong westerly wind bursts (WWB), lasting from a couple of days to two or three weeks. In recent years, the WWBs and their impacts, both local and remote, have been investigated extensively (ZHANG and ROTHSTEIN, 1998; RICHARDSON *et al.*, 1999). It has been suggested that the WWB can generate eastward propagating Kelvin waves, an important factor in the eastern Pacific warming during El Niño

[1] Department of Marine, Earth and Atmospheric Sciences, North Carolina State University, Raleigh, NC, 27695-8208, U.S.A. E-mail: sbao@unity.ncsu.edu

events. As for the local response, it is believed that the WWB could cause the eastward surface jet (YOSHIDA, 1959). Observations have shown that the eastward surface jet is often accompanied by a significant subsurface westward current. During TOGA COARE IOP (Intensive Observation Period) experiment, subsurface westward currents (SSWC) were observed during strong WWB episodes.

The importance of air-sea interaction in seasonal to inter-annual climate prediction is well documented. However, the air-sea coupled processes and their role in mesoscale to synoptic scale weather prediction on time scales from hours to days over the western Pacific warm pool are not well understood. Mesoscale air-sea interaction processes are important in regions with intense convection such as the western Pacific warm pool (SUI *et al.*, 1997).

It is apparent that the ocean and the atmosphere in the tropics communicate on the mesoscale. However, the physical mechanisms are not well understood yet. The progress was limited by the lack of high quality measurements of air-sea fluxes of heat, moisture, and momentum in the warm pool region as well as by the difficulty encountered by coupled models in simulating the air-sea interaction processes over the western Pacific warm pool. In order to achieve a better understanding of the air-sea interaction processes over the western Pacific warm pool, both the availability of high quality measurements and the improvement of air-sea coupled models are necessary. The TOGA/COARE (Tropical Ocean-Global Atmosphere/Coupled Ocean-Atmosphere Response Experiment) was conducted from 1992 to 1993 over the western Pacific warm pool (WEBSTER and LUKAS, 1992). One of its main objectives was to describe and understand the principal processes responsible for the coupling of the ocean and the atmosphere in the western Pacific warm pool system. Data collected during the experiment provided investigators with information for a better understanding of the air-sea interaction processes in the warm pool. However, the development of the fully air-sea coupled models and the numerical experiments of the coupled processes are still limited. It is well known that there is a lag in the ocean's response to the atmospheric forcing. Therefore, a valid question is as to how important the mesoscale air-sea interaction processes are when the ocean's response time scale is much larger than that of the atmospheric forcing.

Our hypothesis is that the precipitation-induced low salinity stable layer may play an important role in the mesoscale air-sea interaction processes. This stable layer tends to isolate the rest of the mixed layer from the surface atmospheric forcing. Consequently, downward transfer of the effects of the surface atmospheric forcing (momentum, heat and salinity fluxes) is impeded by the stable surface layer and their effects effectively limited within the top few meters. Therefore, the thin top layer can respond more effectively to the surface atmospheric forcing. Thus the response could be significantly faster than it would be without the precipitation induced stable surface layer. Existence of the thin top layer in locations with rainfall can also induce mesoscale circulations due to horizontal gradients in sensible heat flux.

It has been observed that precipitation can cause the development of a fresh stable layer at the surface (PRICE 1979; WIJESEKERA *et al.*, 1999). SMYTH *et al.* (1997) observed that associated with this low salinity layer, there is a rapid attenuation of the turbulence below this stable layer; However, the turbulence increases in the precipitation-induced stable layer near the surface. The authors suggested that the turbulence production continues, and the vertical turbulent flux of the turbulent kinetic energy (TKE) is substantially reduced, leading to the decay of the turbulence below the surface precipitation-induced stable layer.

Observations reveal several features of the precipitation-induced fresh stable layer. However, most of the observations were made after the precipitation stopped, and therefore cannot describe the ocean's response during the precipitation. The sampling of rain rates is often made along a track, and thus provides only a one-dimensional description of the oceanic response. Three-dimensional numerical simulation is needed to investigate the temporal and spatial variations of the ocean's response to precipitation.

In this study, three-dimensional numerical simulations of the ocean's response to the westerly wind burst and precipitation are conducted. The simulation results are compared to the observations. The difference in the ocean's response with and without precipitation is investigated. The mechanism by which the atmospheric forcing changes the upper ocean turbulent mixing process is analyzed.

2. Model

POM (Princeton Ocean Model) is used in this study. Developed at Princeton University, it contains an imbedded second moment turbulence closure model to

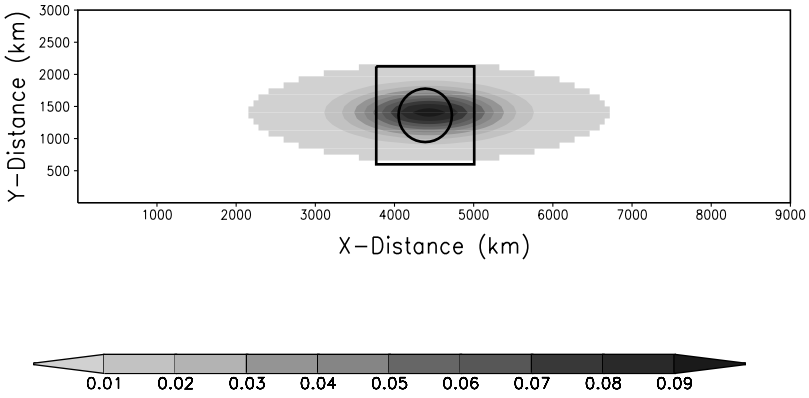

Figure 1
Wind stress (N/m^2) used in Exp. 1. The region enclosed by the inner rectangle is the domain in Experiments 2–5. The area enclosed by the inner circle is the region of the imposed rainfall in Experiments 2–5.

Table 1

Sensitivity experiments

Experiment #	Horizontal grid resolution	Rainfall	Incoming short-wave radiation
1	Coarse (60 km)	Not included	Not included
2	Fine (10 km)	Not included	Not included
3	Fine (10 km)	Included	Not included
4	Fine (10 km)	Not included	Included
5	Fine (10 km)	Included	Included

provide vertical mixing coefficients. It is a sigma coordinate model in that the vertical coordinate is scaled by the water column depth. $\sigma = \frac{z-\eta}{H+\eta}$ is the vertical coordinate. z is the conventional Cartesian vertical coordinate. $D \equiv H + \eta$ where H is the bottom topography that is constant in this study and η is the surface elevation. The horizontal time differencing is explicit whereas the vertical differencing is implicit. The latter eliminates time constraints for the vertical coordinate and permits the use of fine vertical resolution in the surface and bottom boundary layers. The model has a free surface and a split time step. The external mode portion of the model is two-dimensional and uses a short time step based on the CFL condition and the external wave speed. The internal mode is three-dimensional and uses a larger time step based on the CFL condition and the internal wave speed. Complete thermodynamics have been implemented. Details of the model are described by BLUMBERG and MELLOR (1987) and KANTHA and CLAYSON (2000).

The finest horizontal resolution of this simulation is 10 km. A stretching vertical grid scheme is used. Higher vertical resolution is used for the upper layers because the ocean's response to the surface atmospheric forcing such as precipitation associated with squall lines, which last only a few hours, occurs mainly in the upper few meters of the ocean. Below 50 meters, the ocean's response is not significant. In this study, the finest vertical resolution, at the upper-most layer, is about one meter. The external mode time step is 20 seconds, and the internal mode has a time step of 600 seconds.

We assume that the initial temperature and salinity profiles are horizontally homogeneous and the ocean is initially calm with no motion. The temperature and salinity profiles are based on a global data set (LEVITUS *et al.*, 1994; LEVITUS and BOYER, 1994). February monthly average data at 165° E and 5° N are used. This location is the center of the simulation domain.

The parameterization of the turbulent mixing processes is critical in the simulation of the upper ocean boundary layer response to the atmospheric forcing. The second moment turbulent closure model included in POM, often cited in the literature as the Mellor-Yamada turbulent closure model (MELLOR and YAMADA, 1974, 1982), is widely used in geophysical fluid studies because it is relatively simple and still retains much of the second moment accuracy.

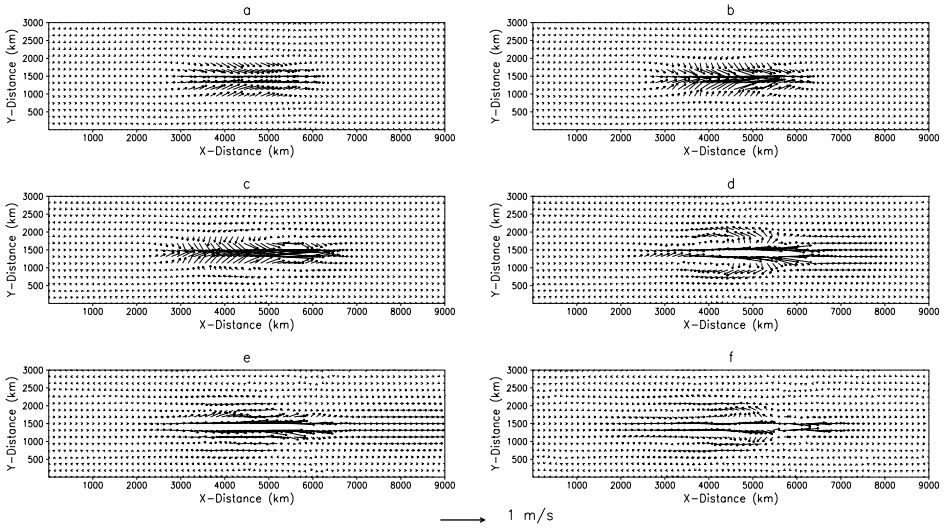

Figure 2
Simulated surface velocity fields in Exp. 1: (a) 3 days, (b) 5 days, (c) 10 days, (d) 15 days, (e) 20 days, (f) 30 days since the beginning of simulation.

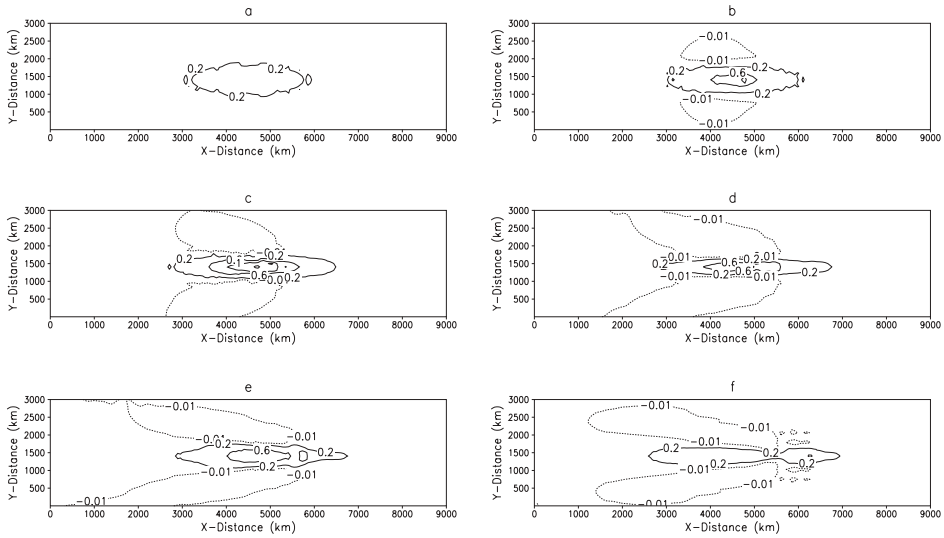

Figure 3
Simulated surface zonal velocity, U (m/s), in Experiment 1: (a) 3 days, (b) 5 days, (c) 10 days, (d) 15 days, (e) 20 days, (f) 30 days since the beginning of simulation. Positive values indicate eastward currents. Note that wind stress is switched off on the 10th day.

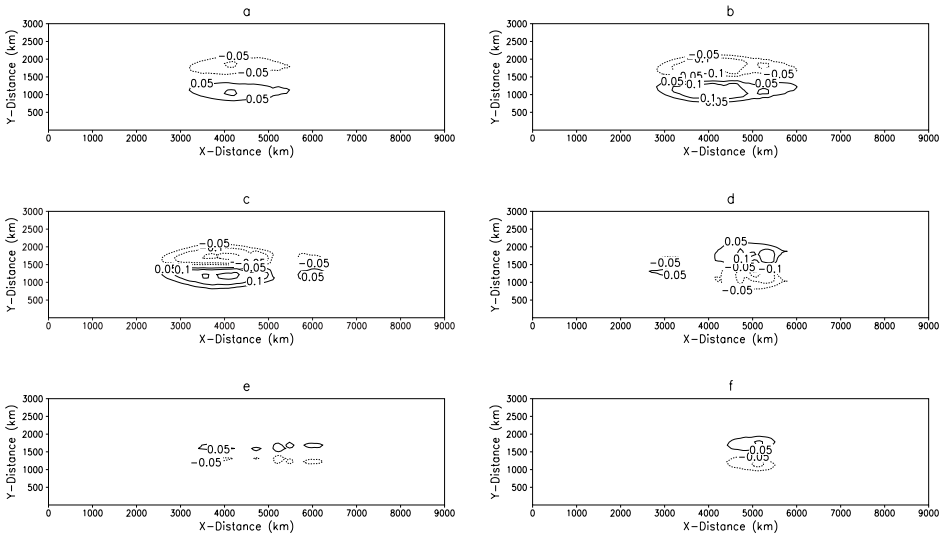

Figure 4
Simulated surface meridional current, V (m/s), in Experiment 1: (a) 3 days, (b) 5 days, (c) 10 days, (d) 15 days, (e) 20 days, (f) 30 days since the beginning of simulation. Note that wind stress is switched off on the 10th day. Positive values indicate the northward currents and the negative values indicate the southward currents.

Turbulent kinetic energy (TKE) and turbulent mixing length are predicted using the following equations:

$$\frac{\partial q^2 D}{\partial t}+\frac{\partial U q^2 D}{\partial x}+\frac{\partial V q^2 D}{\partial y}+\frac{\partial \omega q^2 D}{\partial \sigma} = \frac{\partial}{\partial \sigma}\left[\frac{K_q}{D}\frac{\partial q^2}{\partial \sigma}\right]+\frac{2K_m}{D}\left[\left(\frac{\partial U}{\partial \sigma}\right)^2+\left(\frac{\partial V}{\partial \sigma}\right)^2\right]+\frac{2g}{\rho_0}K_h\frac{\partial \tilde{\rho}}{\partial \sigma}-\frac{2Dq^3}{B_1 l}+F_q \tag{1}$$

$$\frac{\partial q^2 lD}{\partial t}+\frac{\partial U q^2 lD}{\partial x}+\frac{\partial V q^2 lD}{\partial y}+\frac{\partial \omega q^2 lD}{\partial \sigma} = \frac{\partial}{\partial \sigma}\left[\frac{K_q}{D}\frac{\partial q^2 l}{\partial \sigma}\right]+E_1 l\left\{\frac{K_m}{D}\left[\left(\frac{\partial U}{\partial \sigma}\right)^2+\left(\frac{\partial V}{\partial \sigma}\right)^2\right]+E_3\frac{g}{\rho_0}K_h\frac{\partial \tilde{\rho}}{\partial \sigma}\right\}\tilde{W}-\frac{2Dq^3}{B_1}+F_l \tag{2}$$

where $g = 9.8\,\mathrm{m\,s^{-2}}$, q^2 is the turbulent kinetic energy (TKE). ℓ is the turbulent length scale and ω is the velocity component normal to the sigma surface. $\tilde{W} = 1 + E_2(l/kL)$, where von Karman constant $k = 0.4$, $L^{-1} = (\eta - z)^{-1} + (H - z)^{-1}$. $\partial\tilde{\rho}/\partial\sigma \equiv (\partial\rho/\partial\sigma) - (c_s^{-2}\partial p/\partial\sigma)$ where c_s is the speed of sound. B_1, E_1, E_2 and E_3 are constants. U and V are zonal and meridional velocities. F_q and F_l are diffusion terms of q^2 and l, respectively.

The vertical kinematic viscosity and vertical diffusivity, K_m and K_h, are defined according to

$$K_m = qlS_m, \tag{3}$$

$$K_h = qlS_h. \tag{4}$$

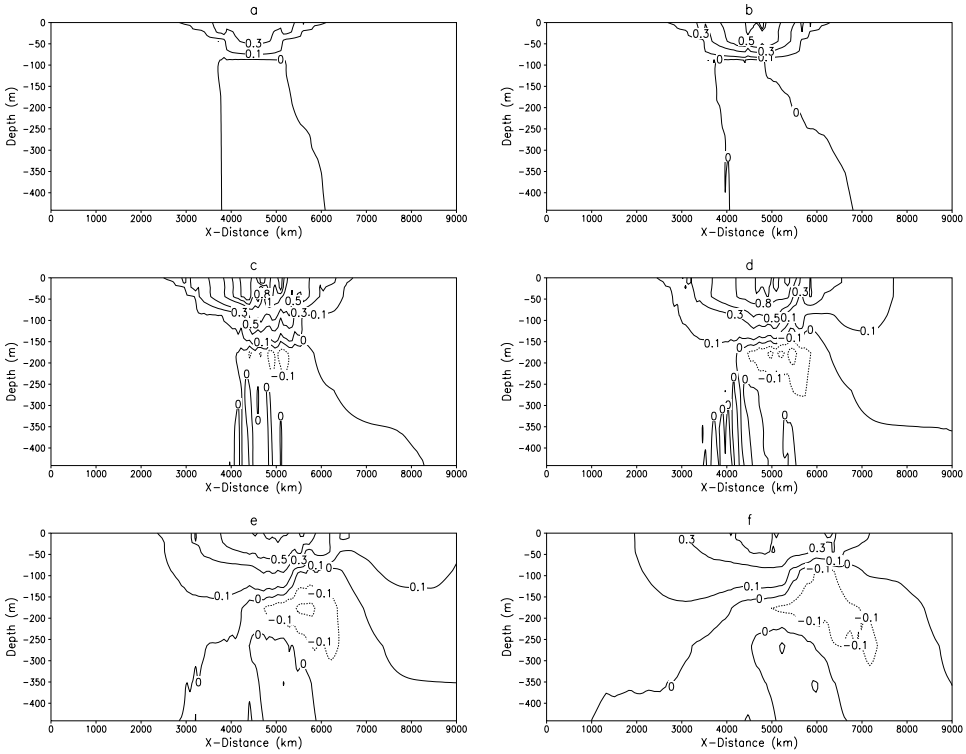

Figure 5
Simulated vertical (*X*-*Z*) cross sections of zonal velocity *U* (m/s) in Experiment 1: (a) 3 days, (b) 5 days, (c) 10 days, (d) 15 days, (e) 20 days, (f) 30 days since the beginning of simulation. Positive values indicate the eastward Yoshida jet. Negative values indicate the subsurface westward jet (SSWJ).

The coefficients, S_m and S_h are functions of Richardson number and K_q is the TKE diffusivity.

During westerly Wind Burst events, the winds over the western Pacific warm pool are mainly zonal. Impact of the meridional wind stress is relatively small compared to the zonal ones (HARRISON and CRAIG, 1993). Therefore, in this study, only idealized zonal wind stress is used. The wind stress field is imposed in the following form (Fig. 1):

$$\tau(x,y) = ramp \cdot \tau_0 \cdot \exp\{-(x - x_0/\Delta x)^2\} \exp\{-(y - y_0/\Delta y)^2\}, \qquad (5)$$

τ_0 is the maximum amplitude of stress. The variable *ramp* varies from 0 to 1 within the first day of the simulation, thus the wind stress is switched on at the beginning of the simulation and is increased to its maximum strength within one day. The same value is then maintained for 10 days and then switched off. (x_0,y_0) is the center of the simulation domain. Δx and Δy are the horizontal grid sizes.

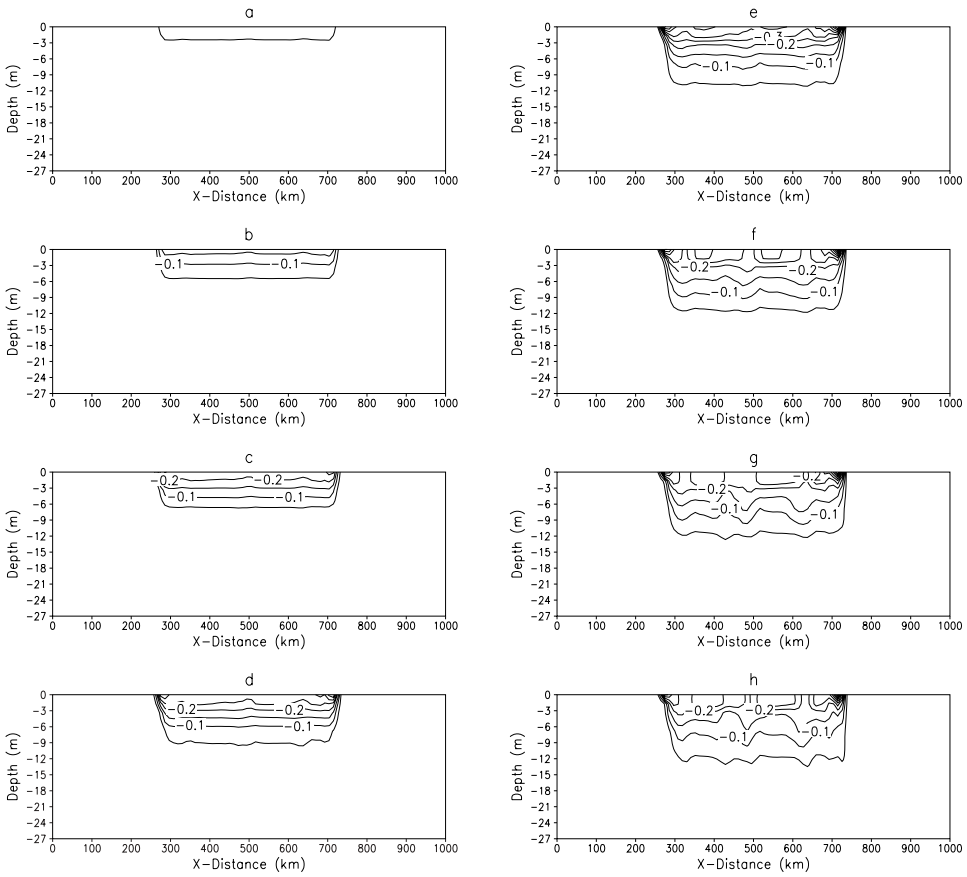

Figure 6
Simulated vertical (*X-Z*) cross sections of the differences between the salinities in Practical Salinity Unit (psu) with and without rainfall (a) 2h, (b) 3h, (c) 4h, (d) 5h, (e) 6h, (f) 7h, (g) 8h, (h) 9h since the beginning of simulation. The negative values indicate the rainfall-induced low salinity layer.

The rainfall-induced salinity flux (F_s) and heat flux (F_t) are given by:

$$F_s = \rho I S_0 \tag{6}$$

$$F_t = \rho C_p I (T_a - T_0) \tag{7}$$

where ρ is the water density, I is the rainfall intensity, S_0 is the surface salinity, C_p is specific heat of liquid water (4218 J K^{-1}/kg), T_a is the atmospheric temperature and T_0 is the sea-surface temperature.

In this study, an idealized precipitation process is considered. The rainfall-induced salinity flux and heat flux are included. The rainfall has an intensity of 15 mm/hour and covers a region enclosed by a circle with a radius of 100 km (Fig. 1). The precipitation process lasts for five hours.

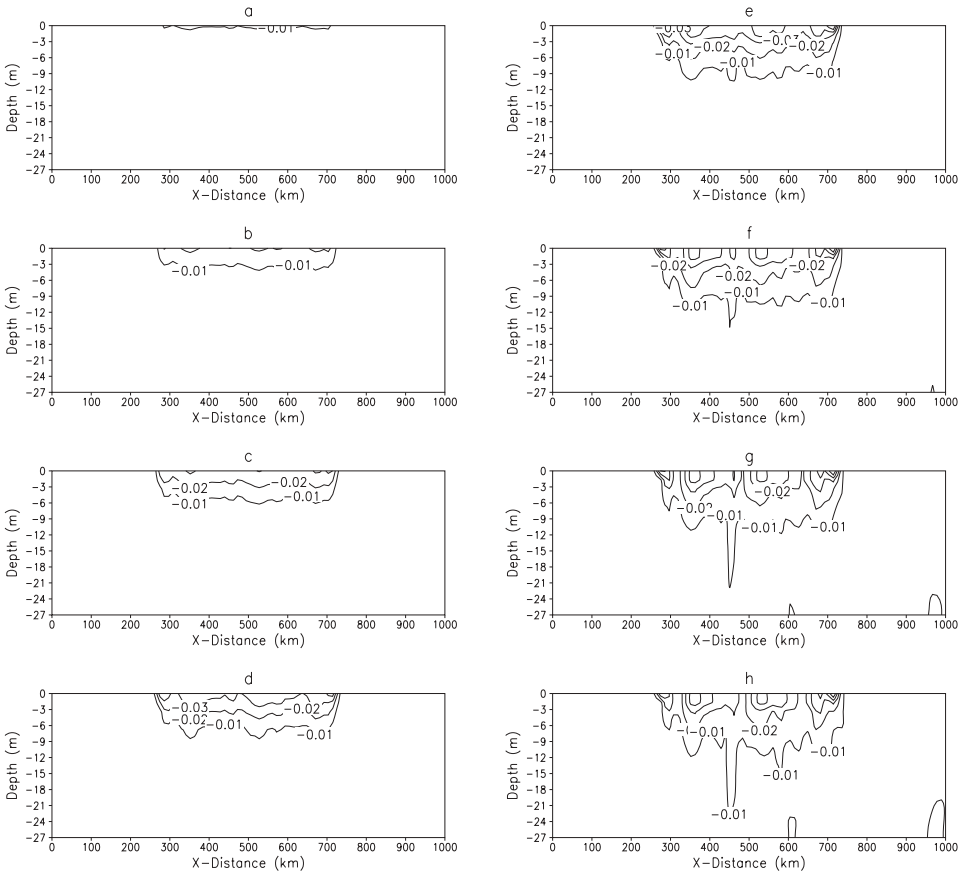

Figure 7
Simulated vertical (*X-Z*) cross sections of the differences between the potential temperature (*K*) with and without rainfall (a) 2h, (b) 3h, (c) 4h, (d) 5h, (e) 6h, (f) 7h, (g) 8h, (h) 9h since the beginning of simulation.

3. Experiment Design

A total of five experiments are conducted to study the effect of precipitation on the upper ocean's response (Table 1). In Exp. 1, the overall features of the Westerly Wind Burst (WWB) and precipitation are simulated with a horizontal resolution of 60 km and a finest vertical resolution of 10 m (top layer). The simulation domain is 9000 km × 3000 km, and the integration time is 30 days. However, the effect of the rainfall on the ocean's response occurs mainly within the top few meters of the ocean. In order to investigate the rainfall-induced effects and their spatial variation, higher resolution numerical modeling is required. In Experiments 2, 3, 4, and 5, the horizontal resolution is 10 km and the finest vertical

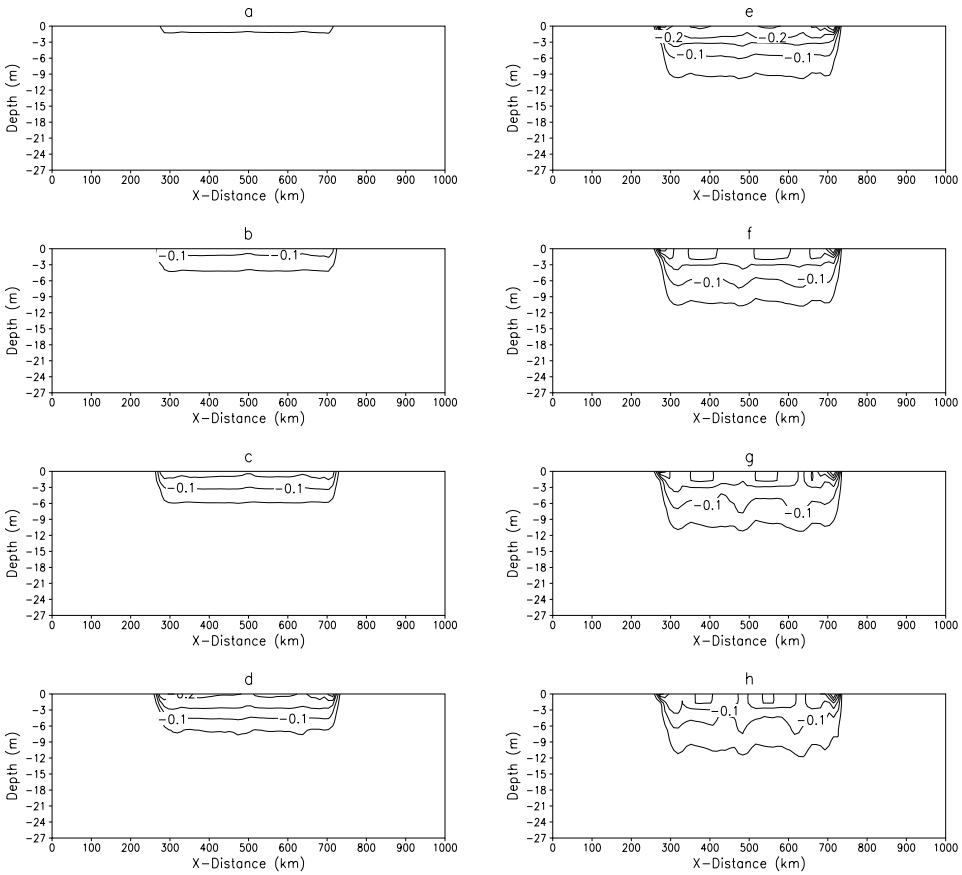

Figure 8
Simulated vertical (*X*-*Z*) cross sections of the differences between density (kg/m^3) with and without rainfall (a) 2h, (b) 3h, (c) 4h, (d) 5h, (e) 6h, (f) 7h, (g) 8h, (h) 9h since the beginning of the simulation. Note that the pattern of the density variation follows that of the salinity variation (see Fig. 6).

resolution within the upper ocean is 1 meter. The domain covers a region of 1000 km $\times$ 1000 km and the integration time is 24 hours in Experiments 2–5. Effects of the precipitation on the mixing processes of the upper ocean are investigated in Experiments 2 and 3. Because the wind stress forcing remains after the formation of the rainfall-induced fresh layer, effects of the precipitation on the vertical transfer of the momentum are investigated. In Exp. 4 and Exp. 5, the effects of rainfall on the vertical transfer of heat flux contributed by short-wave radiation are investigated. In Exp. 4 and Exp. 5, the ocean receives a downward vertical heat flux of 200 W/m^2, a typical value for the location simulated in this study, due to the idealized short-wave radiation.

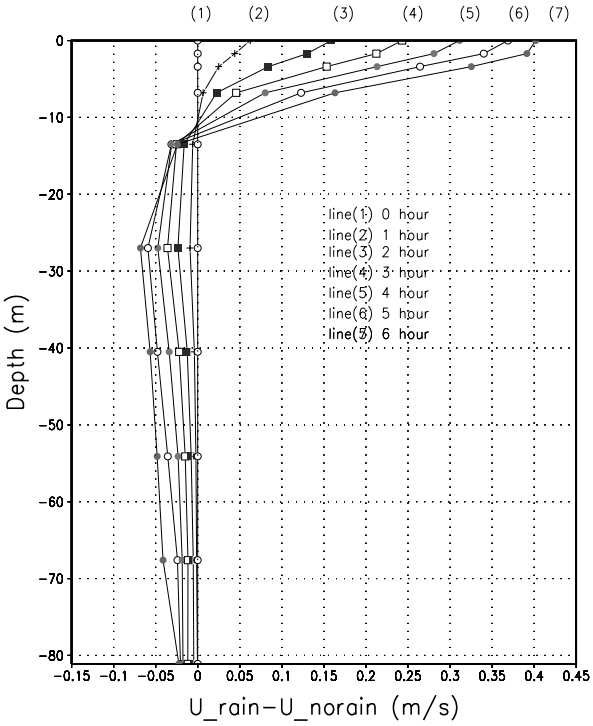

Figure 9
Simulated vertical profiles of the difference between zonal velocities with and without rainfall (U_{rain}-U_{norain}) in m/s, 0–6 hours since the rainfall starts.

4. Results

4.1. Experiment 1: General Features of the Ocean's Response to the Westerly Wind Burst

The wind stress generates an eastward surface Yoshida jet (YOSHIDA, 1959) as indicated in Figures 2 and 3. Time series of the simulation results of the surface velocity fields in Experiment 1 are shown in Figure 2. Time series of the simulation results of the surface zonal velocity, U (m/s), in Experiment 1 are shown in Figure 3. Positive values indicate eastward currents in Figure 3. The wind stress is switched off on the 10th day. The eastward jet increases to its maximum strength in about 10 days, then begins to decrease due to the switch-off of the wind stress. The maximum current reaches a value of 1.5 m/s.

The eastward jet causes meridional current, southward in the Northern Hemisphere and northward in the Southern Hemisphere as shown in Figure 4. The meridional velocities also reach their maximums just after the wind stresses are switched off on the 10th day of the simulation and then begin to decrease. Simulated maximum value of the meridional current is 0.35 m/s.

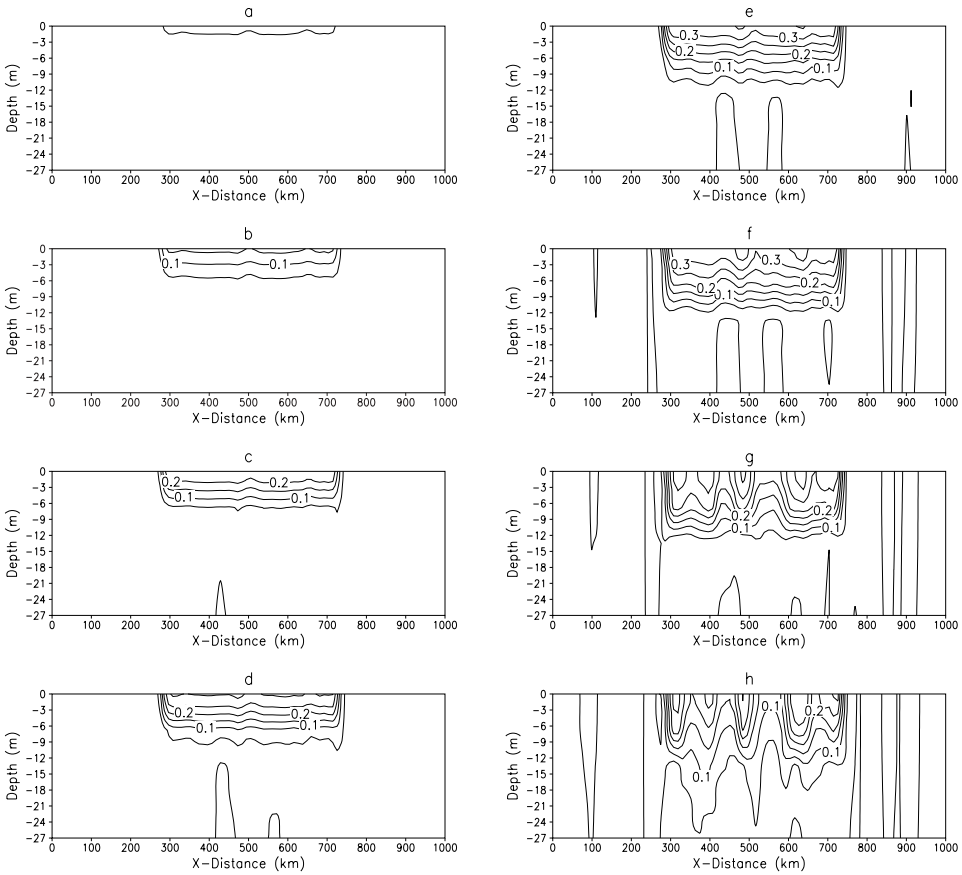

Figure 10
Simulated vertical (*X-Z*) cross-sections of the differences between the zonal velocities, *U* (m/s), with and without rainfall (a) 2h, (b) 3h, (c) 4h, (d) 5h, (e) 6h, (f) 7h, (g) 8h, (h) 9h since the beginning of the simulation.

Vertical *X-Z* cross section of zonal current *U* is shown in Figure 5. The momentum spreads from the surface downward by two major processes: the mean vertical velocity transport and the turbulent flux. The turbulent flux process plays a greater role than the mean velocity transport. The eastward current causes a convergence zone on the leading edge and a divergence zone on the trailing edge. Because of mass continuity, the convergence and divergence caused by the surface eastward jet generate the subsurface westward jet (SSWJ) below the eastward jet. This feature agrees well with the observations (HISARD *et al.*, 1970) and with other simulations such as that by ZHANG and ROTHSTEIN (1998) using a general circulation model originally developed by GENT and CANE (1989).

When the surface wind stress is switched off on the 10th day, there is no energy source to drive the ocean surface current, consequently the surface eastward jet

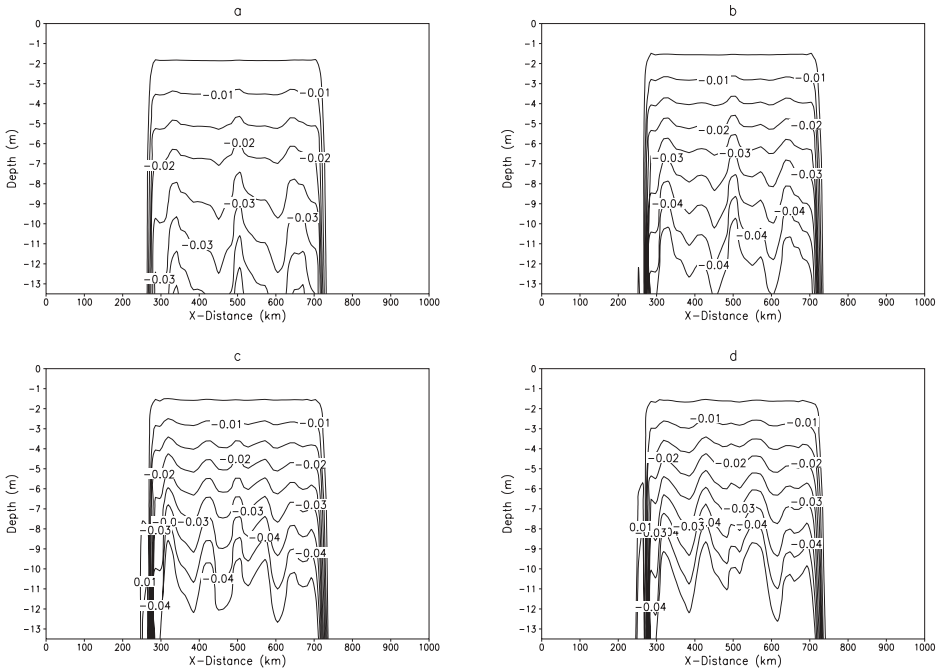

Figure 11
Simulated vertical (*X*-*Z*) cross sections of the differences of the momentum turbulent coefficient K_m (m^2/s) between the simulation results with and without rainfall (a) 2h, (b) 3h, (c) 4h, (d) 5h since the beginning of simulation.

begins to weaken. However, the upwelling and downwelling, which are the energy sources of the SSWJ, still exist. Therefore, from Figure 5, it is apparent that the SSWJ did not begin to weaken immediately after the surface wind stress is switched off. It continues to increase, reaching its maximum on the 15th day, five days after the wind stress is switched off.

4.2. Sensitivity to Rainfall (Experiments 2 and 3)

The (*X Z*) vertical cross section of the differences in the salinity and the potential temperature between the simulation results with and without rainfall (S_{rain}-S_{norain} and T_{rain}-T_{norain}, respectively) are shown in Figures 6 and 7 respectively. It is clear that immediately after the precipitation process started, the negative salinity anomaly and negative temperature anomaly began to develop. The salinity anomaly and the potential temperature anomaly are limited in the region where the precipitation occurred. The magnitudes of the anomalies and the thickness of the rainfall-induced fresh layer continued increasing with time until the precipitation stopped. Then the precipitation-induced layer remains stable near the surface. The magnitudes of the salinity and potential temperature anomalies are the highest near

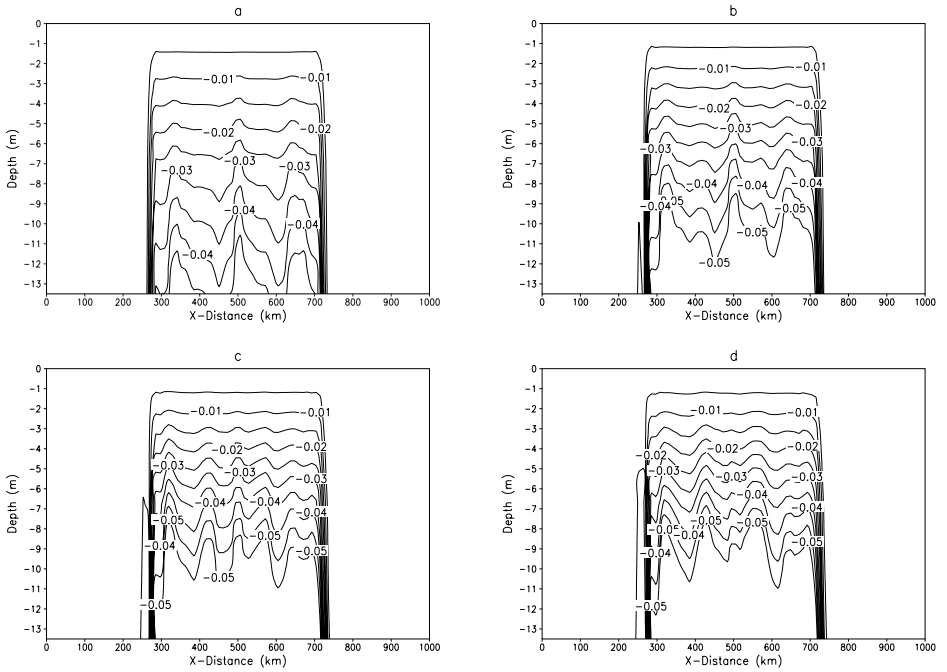

Figure 12
Simulated vertical (*X*-*Z*) cross sections of the differences of the turbulent diffusivity K_h (m^2/s) between the simulation results with and without rainfall (a) 2h, (b) 3h, (c) 4h, (d) 5h since the beginning of simulation.

the surface, and decrease with depth. The maximum salinity anomalies reach 0.3–0.35 psu, and the maximum potential temperature anomalies reach 0.05°C just before the precipitation stops. Four to five hours after the precipitation stops, the magnitudes of the salinity and potential temperature anomalies at a depth of 2–3 meters, reach 0.15–0.2 psu and 0.04–0.05° C, respectively. This rainfall-induced stable layer reaches a depth of about 11–13 meters within a few hours after the precipitation stops.

A rainfall process with similar characteristics (intensity, range and duration) was observed in December, 1992 as part of the Tropical Ocean Global Atmospheres/ Coupled Ocean Atmosphere Response Experiment (TOGA/COARE) in the western Pacific warm pool, at 156°E and 2°S. The observed rainfall-induced negative salinity anomaly reached a magnitude of 0.12 psu near the surface with a depth of about 2–3 meters. The magnitude of the corresponding rainfall-induced negative potential temperature anomaly, measured also at a depth of 2–3 meters, reached 0.05° C at about 5 hours after the formation of the rainfall-induced low salinity stable layer (WIJESEKERA *et al.*, 1999). Thus the simulation results agree well with the observations.

The magnitudes of salinity anomaly and potential temperature anomaly have opposite effects on the density. The negative salinity anomaly tends to reduce the

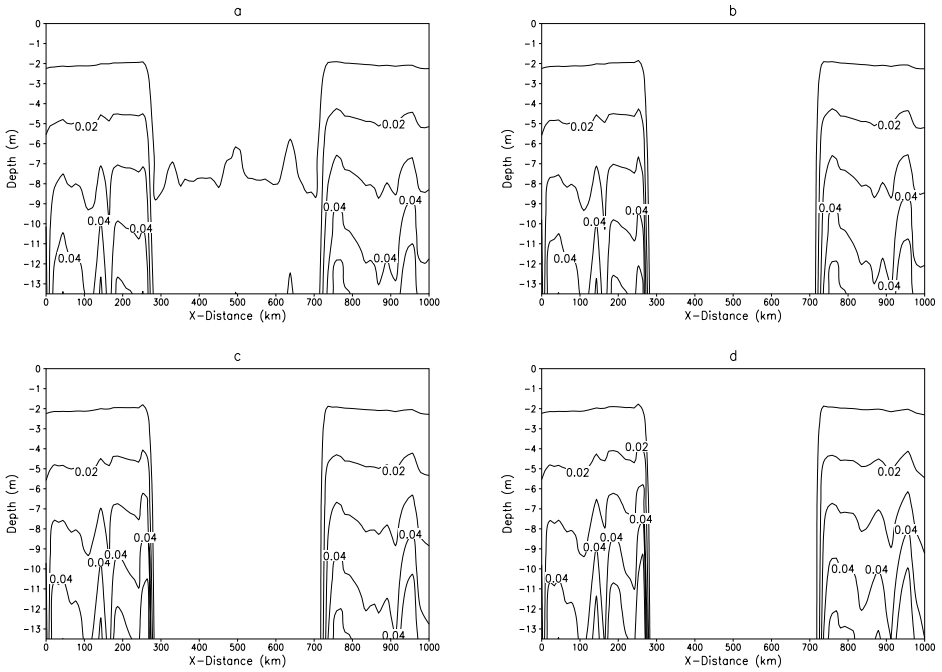

Figure 13
Simulated vertical (X-Z) cross sections of the momentum turbulent coefficient K_m (m^2/s) with rainfall (a) 2h, (b) 3h, (c) 4h, (d) 5h since the beginning of simulation. Note that under the rainfall-covered region K_m values become near zero due to the increased static stability.

density (making the upper layer more stable) while the negative potential temperature anomaly tends to increase the density (making the upper layer unstable). Figure 8 is the (X–Z) vertical cross section of the resulting density anomaly ($\rho_{\text{rain}} - \rho_{\text{norain}}$). It is clear that (the negative) salinity anomaly has the dominant effect on the density. The density anomaly essentially follows the pattern of the salinity anomaly. The maximum magnitude of the density anomaly reached 0.3, or 1.4% of the simulated value with no rain.

The rainfall-induced low salinity, low temperature and low-density layer has a significant effect on the vertical turbulent transport of the momentum from the surface atmospheric forcing. Differences in the vertical current profiles between the no-rain case and the with-rain case (Fig. 9) are analyzed to investigate the effect of the rainfall on the vertical turbulent transport. Horizontal positions of the profiles are at the center of the rainfall region, which is also the center of the simulation domain. It is clear from Figure 9 that immediately after the rainfall started, the zonal velocity near the surface within the rainfall-induced fresh stable layer began to increase, causing significant positive anomaly of U. The magnitude of the U anomaly is at a maximum value of 0.35 m/s near the surface in five hours since the start of the

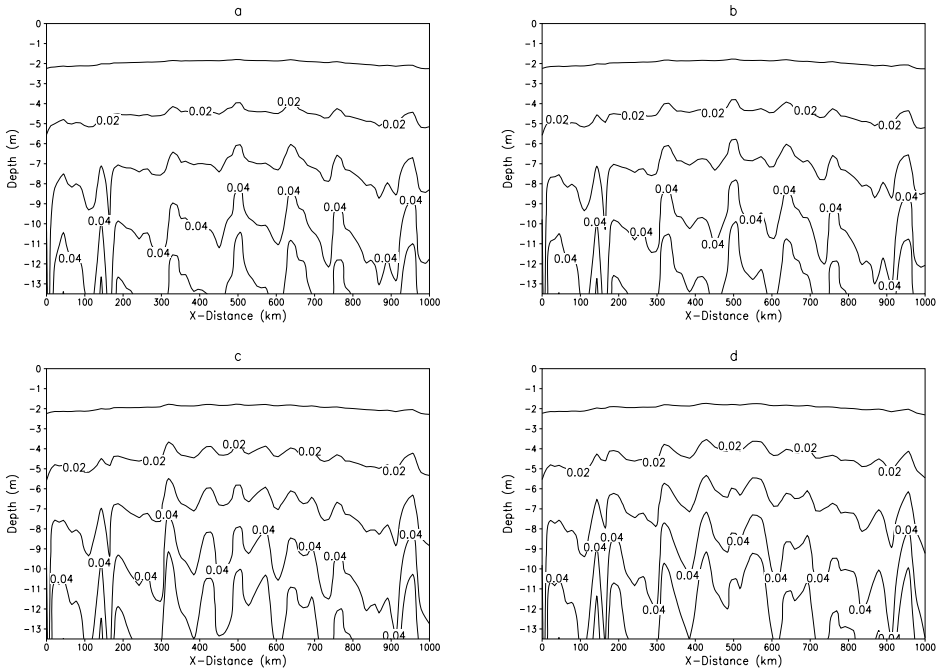

Figure 14
Simulated vertical (*X*-*Z*) cross sections of the momentum turbulent coefficient K_m (m^2/s) without rainfall (a) 2h, (b) 3h, (c) 4h, (d) 5h since the beginning of simulation.

rainfall event. Below a depth of 11–13 meters, which is also the lower boundary of the rainfall-induced fresh stable layer, the anomaly turns negative. The magnitude of the positive anomaly of U near the surface reaches 0.35 m/s at the fifth hour, a 55% increase. It is markedly larger than that of the negative anomaly of U below a depth of 11–13 meters, less than 0.1 m/s, about 10%. Similar features are found in other precipitation regions as shown in the vertical cross-sections of the anomaly of the zonal velocity (U_{rain}-U_{norain}) (Fig. 10).

From Figures 9 and 10, it is clear that the lower part of the rainfall-induced layer acts as a barrier and the effects of the surface atmospheric forcing cannot penetrate it. This process causes that part of the ocean near the surface to respond to the atmospheric forcing much faster than it would without the effects of rainfall.

As mentioned in Section 2 (the model), the vertical turbulent transport terms, which cannot be resolved explicitly and therefore must be parameterized, are given by $\frac{\partial}{\partial\sigma}\left[\frac{K_m}{D}\frac{\partial U}{\partial\sigma}\right]$, $\frac{\partial}{\partial\sigma}\left[\frac{K_h}{D}\frac{\partial T}{\partial\sigma}\right]$ and $\frac{\partial}{\partial\sigma}\left[\frac{K_h}{D}\frac{\partial S}{\partial\sigma}\right]$. The vertical diffusivities of momentum and heat, K_m and K_h, respectively, play an important role in the estimation of the vertical turbulent terms. Vertical cross sections of the anomalies of the simulated K_m and K_h are shown in Figures 11 and 12. It is apparent that the rainfall causes a significant decrease in the values of K_m and K_h. The magnitudes of the anomalies of K_m and K_h

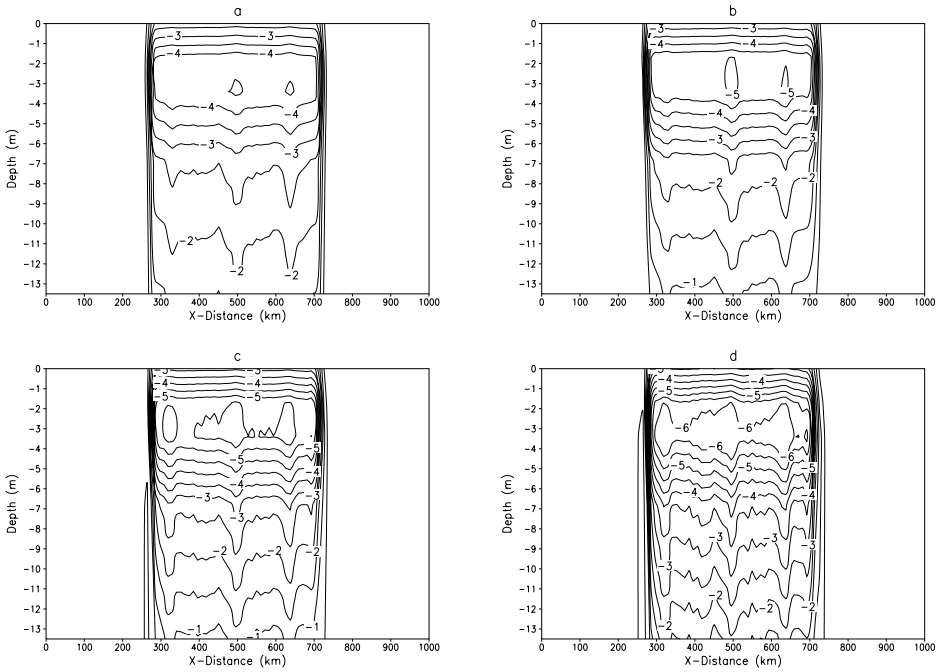

Figure 15
Simulated vertical (*X*-*Z*) cross sections of the differences between the TKE buoyancy production terms (m^2/s^3*10^{-7}) with and without rainfall (a) 2h, (b) 3h, (c) 4h, (d) 5h since the beginning of simulation.

are at their minimum, near zero, at the surface, and increase with depth. At a depth of about 11–13 meters, where the anomaly of U changes sign from positive to negative, the magnitude of K_m anomaly reaches a value of 0.05 m^2/s, or 90% of the value of K_m, in four hours since the rainfall started. K_h anomaly shows a similar pattern; its magnitude reaching a value of 0.065 m^2/s or 90% of the value of the initial K_h, at a depth of about 11–13 meters in four hours after the rainfall starts. Vertical cross sections of K_m with and without rainfall are shown in Figures 13 and 14 respectively.

It appears that the decrease in the simulated vertical diffusivity, K_m, which corresponds to an attenuation of the vertical turbulent mixing, could have caused the effects of the surface atmospheric forcing to be concentrated near the sea surface. Therefore, the effects of the surface rainfall-induced heat flux (cooling), salinity flux, and the wind stress-induced momentum transport can reach a depth of 11–13 meters only. The isolation of the surface rainfall-induced fresh stable layer from the rest of the mixed layer also causes the surface layer to respond to the atmospheric forcing considerably faster.

It will be of interest to investigate as to why the rainfall-induced fresh stable layer tends to attenuate the vertical turbulent mixing. As mentioned in Section 2, the

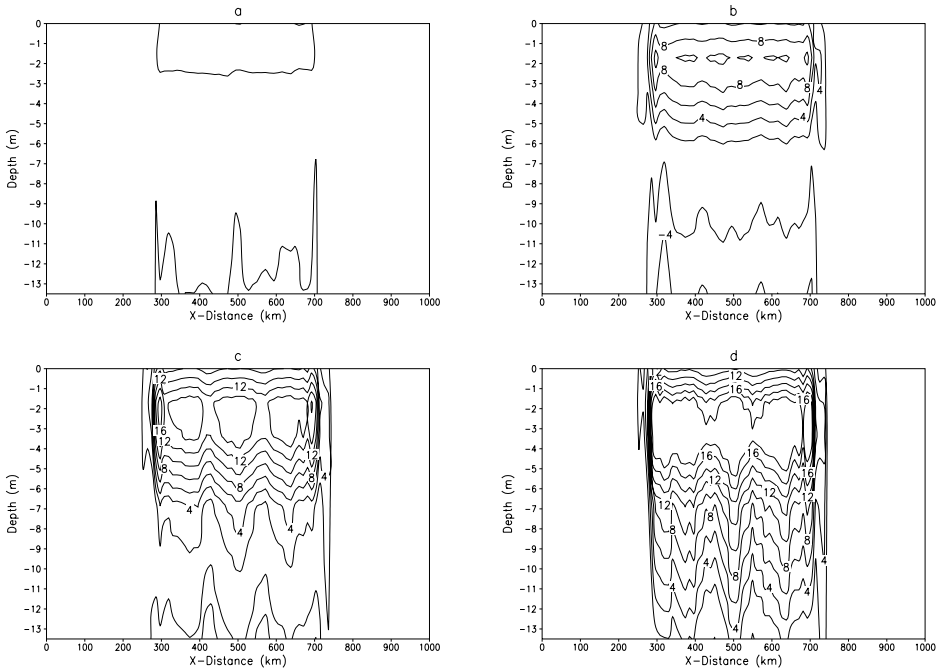

Figure 16
Simulated vertical (*X*-*Z*) cross sections of the differences between the TKE shear production terms (m^2/s^3*10^{-7}) with and without rainfall (a) 2h, (b) 3h, (c) 4h, (d) 5h since the beginning of simulation. Note that the increases in wind shear are due to the concentration of momentum near the ocean surface.

vertical turbulent diffusivities are determined by three factors: Turbulent kinetic energy (TKE), turbulent length scale and Richardson number (Ri). The results of the numerical experiments show that the rainfall-induced fresh stable layer has significant effects on the TKE and Ri.

Equation (1) is used to predict the TKE. The left-hand side has temporal change and horizontal and vertical advection terms. The right-handside terms are, from left to right, the vertical turbulent flux, the shear production, the buoyancy production, and the turbulent dissipation.

In the simulations that have a time scale of a few hours, the advection terms are not as important as other terms. Therefore, the discussion will focus on the production terms (buoyancy and shear), dissipation and the turbulent mixing term.

Due to the presence of the rainfall-induced low density layer, the density gradient increases, leading to an increase in BruntVäisälä frequency, and hence an increase in static stability and a decrease in the buoyancy production of turbulence. Figure 15 shows the vertical cross section of the anomaly of the buoyancy production. It is clear that for depths less than 11–13 meters, the anomaly of the turbulence buoyancy production is negative, apparently caused by the stabilization of the surface fresh

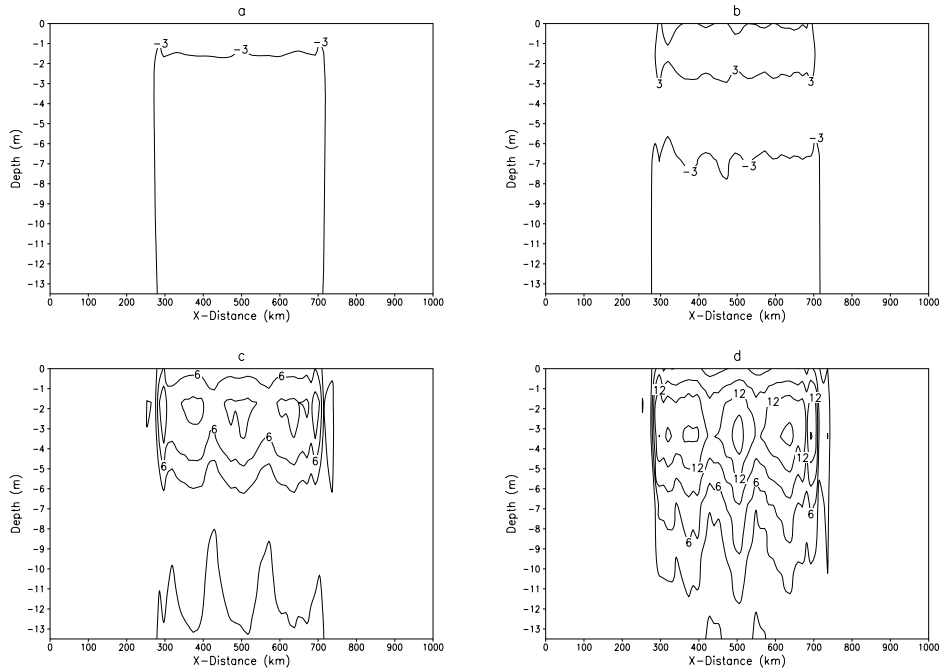

Figure 17
Simulated vertical (*X*-*Z*) cross sections of the differences between the TKE dissipation terms (m^2/s^3*10^{-7}) with and without rainfall (a) 2h, (b) 3h, (c) 4h, (d) 5h since the beginning of simulation.

layer. The magnitude of the anomaly is at maximum at about 3 meters. The maximum anomaly of the buoyancy production term reaches a value of 6×10^{-7} m^2/s^3, at the 4th hour.

At the beginning of the rainfall process, the direct effect of rainfall-induced fresh layer is the stabilization of the upper layer, which tends to decrease the turbulent production. The decrease of the turbulent production leads to the attenuation of the vertical turbulent flux (Figs. 11 and 12), causing the momentum to concentrate near the surface. Consequently, the shear production of turbulence begins to develop, due to the increased velocity gradient between the rainfall-induced fresh layer and the layer below it. Figure 16 is the vertical cross section of the anomaly of shear production term. The magnitude of the positive anomaly of shear production of turbulence is larger than that of the negative anomaly of the buoyancy production of turbulence (Figs. 15 and 16). Thus the rainfall-induced stable layer does not cause the total turbulence production (buoyancy production + shear production) to decrease. However, the increased turbulence also leads to an increase in the turbulence dissipation as shown in Figure 17. The anomaly of the net turbulence production (buoyancy production + shear production – dissipation) is shown in Figure 18. It appears that one hour after the precipitation

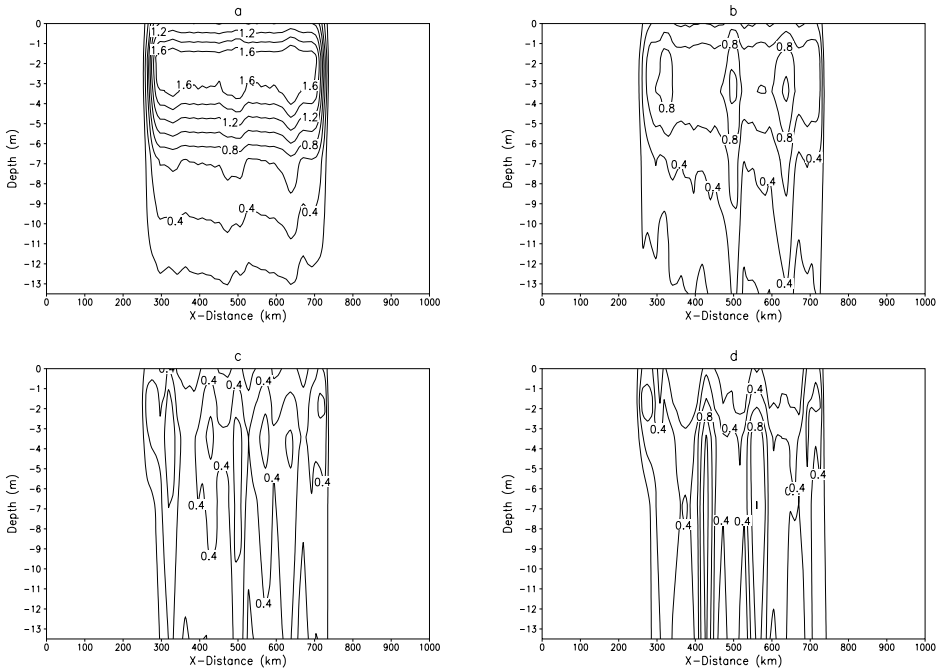

Figure 18
Simulated vertical (*X-Z*) cross sections of the differences between the TKE net production terms (buoyancy production + shear production - turbulence dissipation) (m^2/s^3*10^{-7}) with and without rainfall (a) 2h, (b) 3h, (c) 4h, (d) 5h since the beginning of simulation.

starts, the net turbulence production increases significantly (a positive anomaly) near the surface and decreases (a negative anomaly) below a depth of about 11–13 meters. However, the magnitudes of the anomalies of the net turbulence production decrease quickly in the following hours. The positive anomalies near the surface become 1, 0.8 and 0.6 m^3/s^3 at the second, third and fourth hours, respectively. The simulated negative anomalies are not as coherent as at the beginning of the rainfall. The decrease in the magnitudes of the anomalies shows that the effect of the rainfall-induced stable fresh water layer on the net turbulence production is diminishing rapidly.

Vertical cross section of the anomaly of the TKE is shown in Figure 19. Comparing Figure 18 with Figure 19, it is clear that with the decrease in the effect of the rainfall-induced fresh stable layer on the net turbulence production, the magnitude of the anomalies of the TKE increases significantly. This means that in addition to the effects on the net turbulence production, the vertical turbulent flux term (the first right-hand term in TKE equation (1)) also appears to be an important factor in determining the variation of turbulence due to the rainfall. Vertical cross section of the anomaly of the vertical diffusivity K_q is shown in Figure 20. Similar to

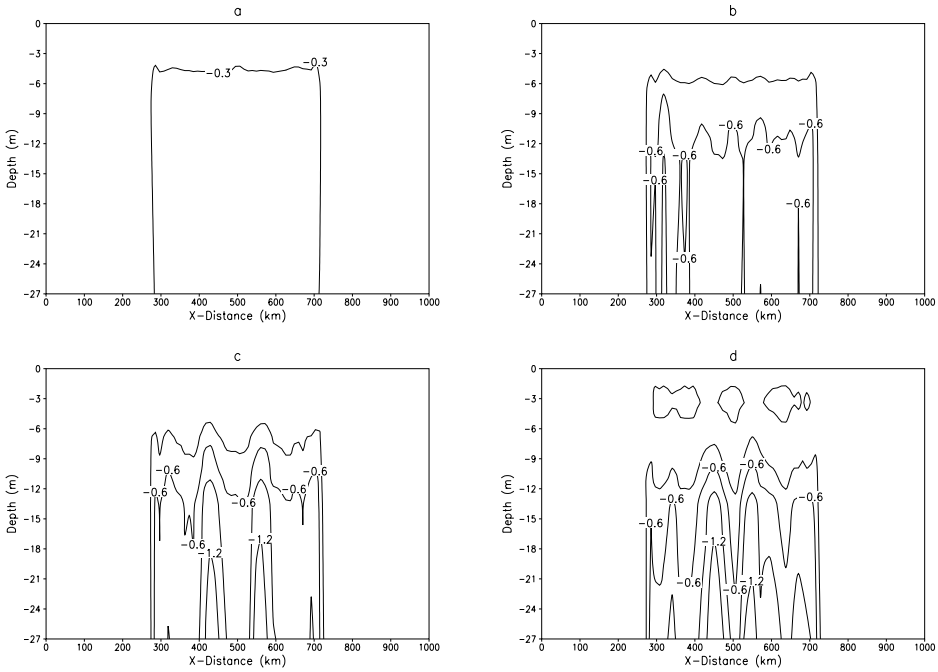

Figure 19
Simulated vertical (*X*-*Z*) cross sections of the differences between TKE (m^2/s^2*10^{-3}) with and without rainfall (a) 2h, (b) 3h, (c) 4h, (d) 5h since the beginning of simulation.

the momentum, the turbulence that is transported downward to depths below 11–13 meters also decreases. More turbulence is concentrated near the surface causing the turbulence near the surface to increase. After becoming disconnected from its source above, the turbulence below 11–13 meters decreases significantly.

In addition to TKE, the stability parameter Richardson number (Ri) is also affected by the rainfall. Ri is actually the ratio of buoyancy production to the shear production. Figure 21 is the vertical cross section of the anomaly of Ri. Before the rainfall starts, the uppermost few meters are well mixed without significant density gradient, thus Ri is close to zero near the surface. One hour after the rainfall started, due to the stratification induced by the rainfall, Ri increases drastically, reaching a maximum value of 0.35 and remaining positive through the rainfall-induced fresh layer. However, in later hours, due to the increase in the simulated velocity shear, the effects of the dynamic instability increase rapidly. After the end of the rainfall, the source of fresh water does not exist, while the wind stress continues to provide momentum, causing stronger velocity shear. Consequently, the Ri dropped to a value below 0.25 (Fig. 21), the critical Richardson number. This means that the effect of the shear on the TKE production is larger than the effect of the rainfall-induced

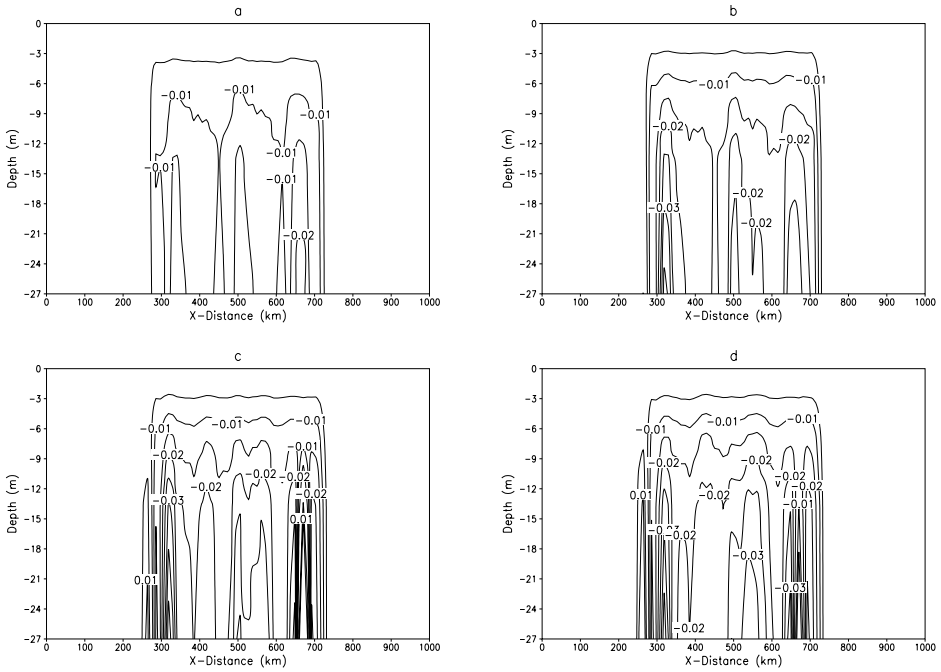

Figure 20
Simulated vertical (*X*-*Z*) cross sections of the differences of the TKE diffusivity coefficient K_q (m^2/s) with and without rainfall (a) 2h, (b) 3h, (c) 4h, (d) 5h since the beginning of simulation.

stratification. This agrees with the simulation results discussed above that the turbulence production continues even after the end of the rainfall.

Although the R_i is under the critical Richardson number, which means the shear-induced dynamic instability is still dominant, the rainfall-induced stratification significantly effects the vertical diffusivities, K_h and K_m, through the functions, S_h and S_m, in (see equations (3) and (4) in Section 2, the model). The rainfall-induced fresh layer causes the stability functions S_h and S_m to decrease drastically (Figures 22 and 23). The details of the calculation of S_h and S_m are available from MELLOR and YAMADA (1982).

The anomaly of stability-related functions S_h and S_m in equations (3) and (4), combined with the anomaly of turbulence kinetic energy, result in a significant decrease in the simulated vertical turbulent flux diffusivities, K_h and K_m (Figs. 11, 12, 13 and 14). The magnitudes of the negative anomaly of turbulent diffusivities are small near the surface. At a depth of 11–13 meters, the magnitudes of the anomalies reach 90%. This appears to be the reason that the turbulence caused by the surface atmospheric forcing due to the salinity flux and the momentum flux cannot propagate below a depth of 11–13 meters. The fresh layer is thus isolated from the rest of the ocean and its response to the atmospheric forcing becomes decidedly more rapid.

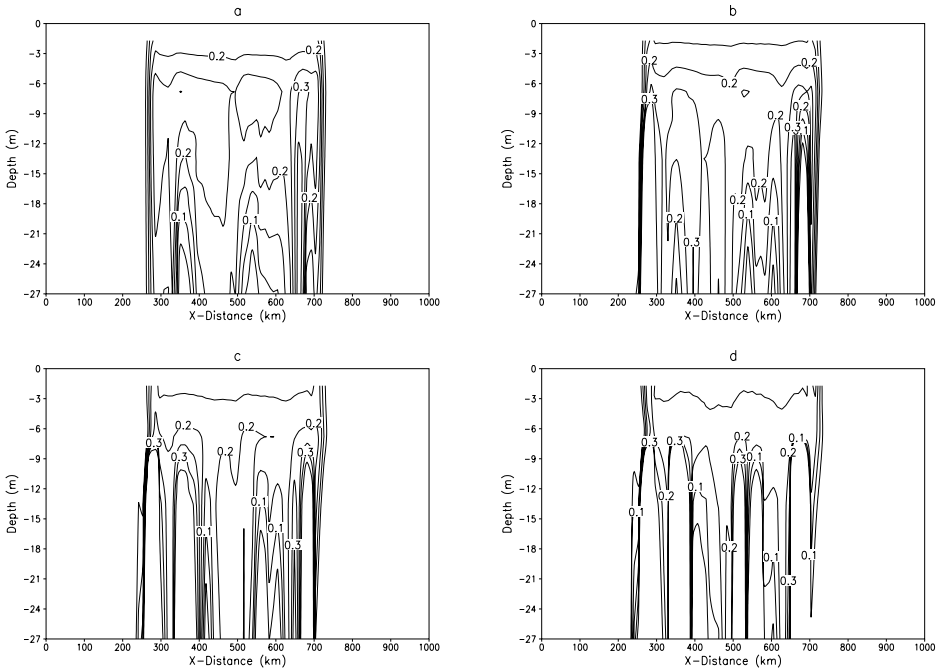

Figure 21
Simulated vertical (*X-Z*) cross sections of the differences between Richardson number with and without rainfall (a) 2h, (b) 3h, (c) 4h, (d) 5h since the beginning of simulation.

4.3. Sensitivity to the Short-wave Radiation Warming (Experiments 4 and 5)

The results of the numerical experiments 2 and 3 show that K_h, the vertical heat diffusivity, experienced similar variation to K_m, the vertical momentum diffusivity. It is believed that the surface downward heat flux, such as the short-wave radiation after the rainfall, an important mechanism in air-sea interaction, may act similarly to the momentum flux. That is, the heat may also concentrate near the surface, without being transferred downward. An experiment is carried out to examine the rainfall-induced fresh layer's effect on the downward heat fluxes. A short-wave radiation that contributes to a downward vertical heat flux of 200 W/m^2 to the ocean is imposed on the surface after the rainfall stopped, and the warming continued for four hours (Exp. 5).

In a companion experiment, the same short-wave warming is imposed with the same configuration except that there is no rainfall (Exp. 4). Increase of the sea-surface temperature ($SST_{norain} - SST_{norain_{t=0}}$) due to the short-wave radiation warming without rainfall (Exp. 4) is shown in Figure 24. Increase of the sea-surface temperature due to the short-wave radiation warming with rainfall is shown in Figure 25. From Figures 24 and 25, it is apparent that without rainfall, the

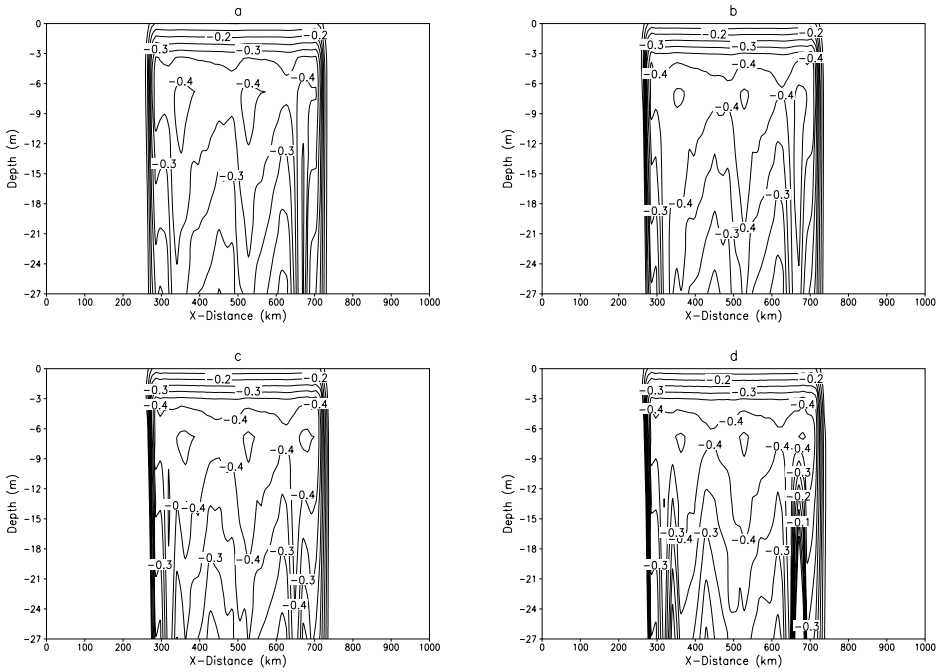

Figure 22
Simulated vertical (*X-Z*) cross sections of the differences between the values of S_h with and without rainfall (a) 2h, (b) 3h, (c) 4h, (d) 5h since the beginning of simulation.

increase in SST due to the short-wave radiation reaches a maximum value of only 0.035° C. In addition, the warming effect does not last long. In four hours, the warming effect has become insignificant. In the case with rainfall, the increase in SST reaches a maximum value of 0.13° C, nearly three times more than that without rainfall. In addition, the warming effect lasts significantly longer than that without rainfall. On the fourth hour since the start of the short-wave radiation, the positive SST anomalies are still significant and coherent. It is clear that due to the inclusion of the rainfall, the simulated K_h decreases, as mentioned before (Fig. 12), and the short-wave radiation warming is concentrated near the surface. The rainfall-induced fresh layer responds to this warming much more rapidly than the rest of the ocean below it.

5. Conclusions

Because of a lack of adequate observations on the western Pacific warm pool region during convective precipitation, numerical simulations provide an important

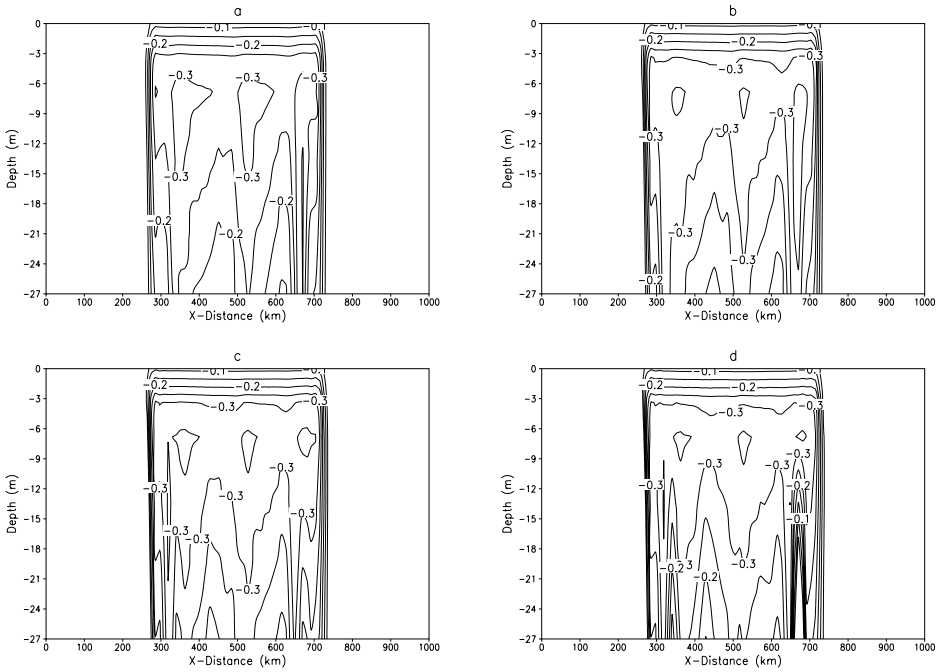

Figure 23
Simulated vertical (*X*-*Z*) cross sections of the differences between the values of S_m with and without rainfall (a) 2h, (b) 3h, (c) 4h, (d) 5h since the beginning of simulation.

approach to study the air-sea interaction processes. The simulations reproduced ocean's response to the precipitation, such as the formation of a fresh layer and surface cooling, which agree well with the observations. The precipitation-induced fresh layer can cause the vertical turbulent diffusivities to diminish at a depth of about 11–13 meters within a few hours. The concentration of the surface wind stress-induced momentum near the surface produces an increase in the velocity shear, which, in turn, causes significant dynamic instability and turbulence increases near the surface. Hence when there is precipitation, the ocean appears to respond to the surface atmospheric forcing much faster than it would without rainfall. These idealized simulation results are in agreement with the observations of sea surface temperature and salinity after a rainfall event of similar characteristics during TOGA COARE in December 1992 (WIJESEKERA *et al.*, 1999).

Although the results of this study support the hypothesis that rainfall can induce the upper ocean to respond to atmospheric forcing more rapidly, than it would without rainfall, further studies are still needed to fully understand the air sea interaction mechanisms. One of the inadequacies of this study is that only the

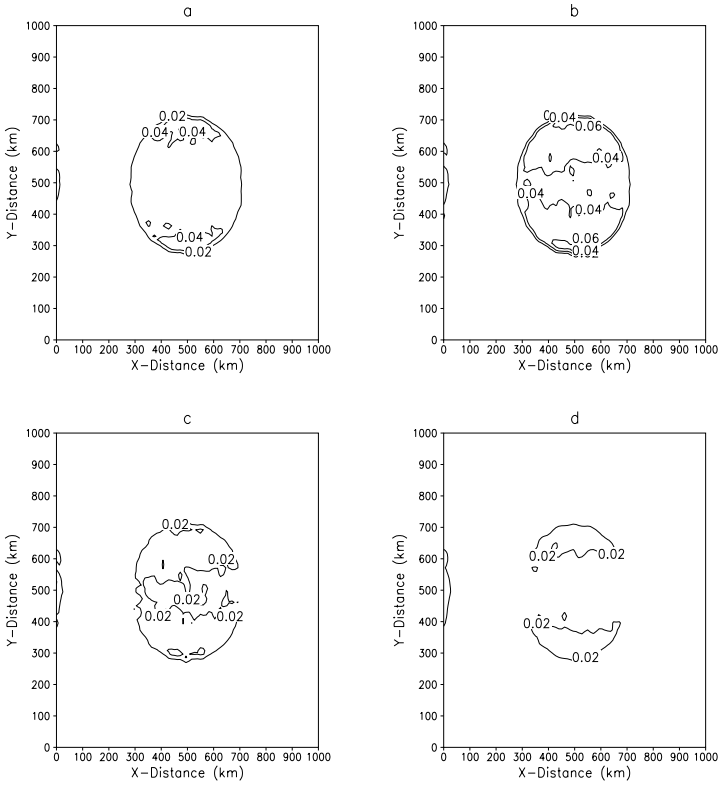

Figure 24
Simulated SST (*K*) anomalies due to the short-wave radiation with no rainfall in Exp. 4 (a) 1h, (b) 2h, (c) 3h, (d) 4h since the beginning of the experiment.

atmospheric effects on the ocean are considered. The ocean's feedback is not included. To fully understand the air-sea interaction processes, a two-way coupled model is required.

Acknowledgements

This work was supported by the Division of Atmospheric Sciences, National Science Foundation under grant No. ATM-9632390, ATM-0080088, and National Oceanic and Atmospheric Administration under Grant No. NA16RP2543. The model simulations were performed in the North Carolina Super Computing Center, Research Triangle Park, NC.

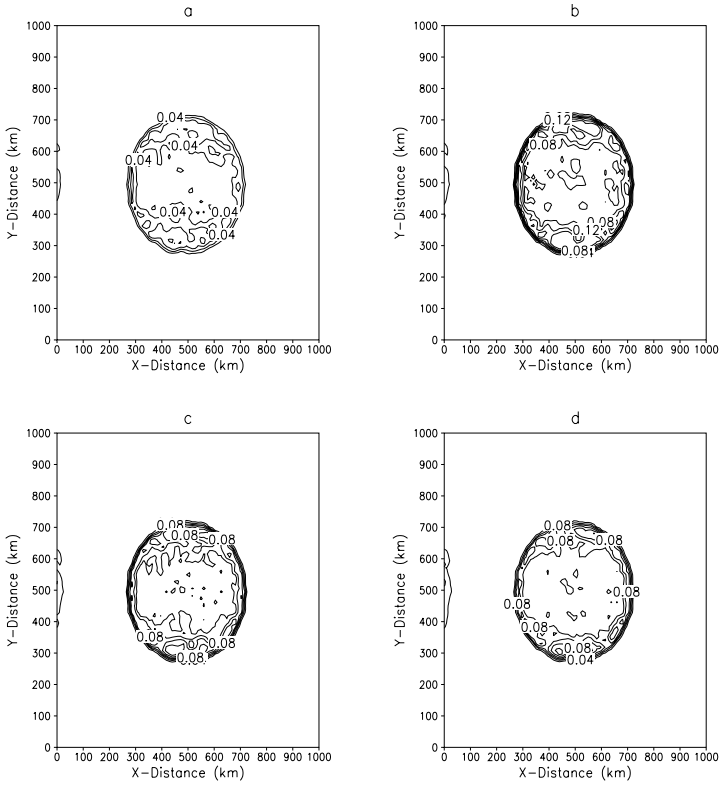

Figure 25
Simulated SST (*K*) anomalies due to the short-wave radiation with rainfall in Exp. 5 (a) 1h, (b) 2h, (c) 3h, (d) 4h since the beginning of the experiment.

References

Blumberg, A. F. and Mellor, G. L. (1987), *A description of a three-dimensional coastal ocean circulation model*. In: *Three-dimensional Coastal Ocean Models* (ed. N. Heaps) American Geophysical Union, 208 pp..

Gent and Cane (1989), *A Reduced Gravity, Primitive Equation Model of the Upper Equatorial Ocean* J. Comput. Phys. *81*, 444–481.

Harrison, D. E. and Craig, A. P. (1993), *Ocean Model Studies of Upper-ocean Variability at 0°, 160°W during the 1982–83 ENSO: Local And Remotely Forced Response*. J. Phys. Oceanogr. *23*, 425–451.

Hisard, H., Merle, J., and Vioturiez, B. (1970), *The Equatorial Under Current at 170°E in March and April 1967*, J. Mar. Res. *28*, 128–303.

Kantha, L. H. and Clayson, C. A., *Numerical Models of Oceans and Oceanic Processes*. Academic Press, 2000.

Zhang, K. Q. and Rothstein, L. M. (1998), *Modeling the Oceanic Response to Westerly Wind Bursts in the Western Equatorial Pacific*. J. Phys. Oceanogr. *28*, 2227–2249.

Levitus, S. and Boyer, T. P. (1994), *World Ocean Atlas 1994*, Volume 4: Temperature, NOAA Atlas NESDIS 4, 11 pp.

Levitus, S., Burgett, R., and Boyer, T. P. (1994), *World Ocean Atlas 1994*, Volume 3: Salinity. NOAA Atlas NESDIS 3, 99 pp.

MELLOR, G. L. and YAMADA, T. (1982), *Development of a Turbulent Closure Model for Geophysical Fluid Problems*, Rev. Geophys. *20*, 851–875.

PRICE, J. R. (1979), *Observations of a Rain-formed Mixed Layer*, J. Phys. Oceanogr. *9*, 643–649.

RICHARDSON, R. A., GINIS ISSAC and ROTHSTEIN, L. M. (1999), *A Numerical Investigation of the Local Ocean Response to Westerly Wind Burst Forcing,* in the Western Equatorial Pacific, J. Phys. Oceanogr. *29*, 1334–1352.

SMYTH, W. D., ZAVIALOV, P. O. and MOUM, J. N. (1997), *Decay of Turbulence in the Upper Ocean Following Sudden Isolation from Surface Forcing*, J. Phys. Oceanogr. *27*, 820–822.

SUI, C. H., LI, X., LAU, K.-M., and ADAMEC, D. (1997), *Multiscale Air–Sea Interactions during TOGA COARE*, Month. Weat. Rev. *125*, 4, 448–462.

WEBSTER, P. J. and LUKAS, R. (1992), *TOGA COARE: The Coupled Ocean-Atmosphere Response Experiment*, Bull. Amer. Meteor. Soc. *73*, 1377–1416.

WIJESEKERA, H. W., PAULSON, C. A., and HUYER, A. (1999), *The Effect of Rainfall on the Surface Layer in the Western Equatorial Pacific during a Westerly Wind Burst*, J. Phy. Oceanogr. *29*, 612–632.

YOSHIDA, K. (1959), *A Theory of the Cromwell Current (the Equatorial Undercurrent) and of the Equatorial Upwelling*, J. Oceanogr. Soc. Japan *15*, 159–170.

(Received January 9, 2002, accepted June 7, 2002)